Numerical Study on the Hydrodynamics of a Self-Heating Biomass Fast Pyrolysis Reactor

3 **AUTHORS**, INCLUDING:

huiyan zhang
Southeast University (China)
56 PUBLICATIONS   **1,144** CITATIONS

SEE PROFILE

Rui Xiao
China Institute for Radiation Protection
170 PUBLICATIONS   **2,721** CITATIONS

SEE PROFILE

Numerical Study on the Hydrodynamics of a Self-Heating Biomass Fast Pyrolysis Reactor

Huiyan Zhang, Shanshan Shao, Rui Xiao,* Qiwen Pan, Ran Chen, and Jubing Zhang

School of Energy and Environment, Southeast University, Nanjing 210096, People's Republic of China

ABSTRACT: A novel, self-heating biomass fast pyrolysis reactor named internally interconnected fluidized beds (IIFB) was proposed for the efficient production of bio-oils and chemicals by catalytic fast pyrolysis of biomass. The IIFB reactor mainly consisted of a pyrolysis bed (biomass pyrolysis) and a combustion bed (char burning and catalyst regeneration) connecting through a draft tube and a dipleg. Each bed was designed for the continuous operation. The hydrodynamic characteristics of the reactor, such as solid circulation rate, pressure distribution, and volume fraction of particles were performed using numerical simulation in this study. A non-steady-state, Eulerian multi-fluid model was used. The gas phase is modeled with a $k-\varepsilon$ turbulent model, and the particle phase is modeled with the kinetic theory of granular flow. The experiments were carried out in an IIFB experimental system to verify the model. The simulation results show that the solid circulation rate was kept as a constant of 110 kg/h after 12 s of computational time compared to the value of 104.5 kg/h obtained in the experiments. The time-averaged values of the pressures at different positions after 12 s of computational time were also close to the experimental data. The particles in the dipleg were monitored to drop downward at a uniform speed of 0.07 m/s. In comparison to that in the draft tube, the velocity magnitude (including vertical or horizontal directions) of the particles decreased along the height of the draft tube, whereas the vertical velocity of the particles first underwent a disturbed flow because of the solid—solid and solid—wall collisions, then increased rapidly, and last were kept at an almost uniform magnitude. The results can provide a conceptual guide for designing, building, and operating the system of biomass (catalytic) fast pyrolysis.

1. INTRODUCTION

The shortage of fossil fuels, especially petroleum resources, is stimulating the interest to search for renewable energy to substitute for traditional fuels.[1−3] Lignocellulosic biomass is the most abundant and the renewable source of carbon, which can be converted into liquid fuels and chemicals.[4,5] However, biomass is a low-energy-density resource compared to fossil fuels, which make transportation, storage, and handling more costly per unit of energy.[6] Biomass fast pyrolysis (BFP) can convert biomass to considerable liquid fuel, named as bio-oil, which can reduce transport cost up to 87%. BFP is a simple and inexpensive technology for biomass conversion.[7] It has been shown to be 2−3 times cheaper than biomass conversion technologies based on gasification and fermentation processes.[8]

During the last 20 years, several types of reactors, e.g., fluidized beds, transported and circulation fluidized beds, spouted beds, and ablative and vacuum pyrolysers, have been developed for the BFP process.[9−16] The pyrolysis process is an endothermic reaction; heat is required for biomass pyrolysis. To increase the economic potential of BFP, pyrolysis char is usually combusted to serve the heat needed in the process. Recently, BFP with catalysts, called catalytic fast pyrolysis (CFP), has attracted numerous interests because of the versatility and potential of sustainable production of liquid fuels and chemicals. However, the catalysts are deactivated obviously and need to be regenerated in a regeneration bed.[17−24] Externally interconnected fluidized beds (EIFB) reactor has been used for the BFP process and catalyst regeneration.[12,25] The char, catalyst, and sand are separated from pyrolysis gas by the cyclone separator and sent back into the combustion bed. However, it requires a high separating

efficiency of the cyclone separator or more cyclone separators.[26] Furthermore, the solid circulation between the pyrolysis bed and combustion bed is difficult to control.

To overcome these problems, we proposed a novel reactor, internal interconnected fluidized beds (IIFB). The IIFB reactor can realize a three-in-one process: CFP of biomass, regeneration of catalyst, and energy reduction by direct heat transfer. Its configuration and working principle are shown in Figure 1. The IIFB reactor has two beds, i.e., a pyrolysis bed (the draft tube and fountain region) and a combustion bed (the annulus), separated by a draft tube and conical dipleg. Mass and heat are transferred through slots at the bottom of the draft tube. Biomass is fed into the draft tube with N_2 or noncondensable gas produced from biomass pyrolysis through the bottom of the reactor. Hot particles (sand/catalyst/their mixture) are introduced into the draft tube from the combustion bed through the slots. The bed materials transfer heat rapidly to biomass, increase the temperature, and lead to (catalytic) fast pyrolysis in the draft tube. In the fountain region, char and bed materials separate from pyrolysis vapors because of their gravity, fall into the dipleg, and then slip into the combustion bed. Some small particles that are blown out of the pyrolysis bed are captured by a cyclone and recycled into the combustion bed. In the combustion bed, the high carbon-containing char is combusted and releases heat to the bed materials. The heated bed materials in the combustion bed are entrained into the draft tube again.
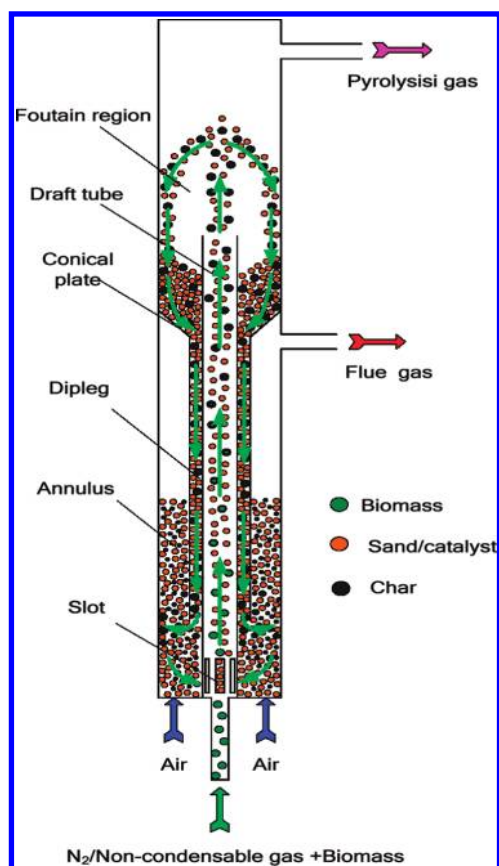
Figure 1. Working principle of the internally interconnected fluidized beds for biomass (catalytic) fast pyrolysis.

During the CFP process, the used catalyst can be regenerated in the combustion bed of the reactor and used to replenish the necessary amount of catalysts continuously. The IIFB reactor has a simpler structure, lower energy consumption, and lower investment compared to the EIFB reactor. Above all, the solid circulation rate can be controlled more easily by adjusting the spouting and fluidizing gas flow rates.

We have carried out some experimental works about flow pattern and pressure drop of the IIFB reactor.[27] The optimizing conditions for operating it have been obtained. However, the hydrodynamics of the reactor are different with a traditional fluidized bed and spout-fluidized bed. The flow behaviors of this reactor are more complicated. More information about the flow behaviors, such as the pressure and particle velocity distributions in the IIFB reactor, should be studied. Nowadays, numerical simulation has become very popular in a gas—solid two-phase flow study.[28] It is a powerful and attractive alternative for obtaining detailed information about flow behaviors and the scale-up relationships of a reactor. Thus, numerical models can be built, and the hydrodynamics can be further studied using the numerical simulation method to obtain more detailed information of the IIFB reactor.

In this work, a three-dimensional, multi-fluid Eulerian model incorporating the kinetic theory for solid particles is used to simulate the gas—solid flow of the new reactor. The pressure and velocity magnitude, volume fraction of particles, and solid circulation rate at typical conditions were investigated. Besides, the simulation results were compared to the experimental results to verify the numerical model. The solid circulation rate, which determines the handling capacity of the reactor, is another important flow parameter. We investigated it in an IIFB experimental system under the optimizing conditions for comparison to the simulation results.

2. NUMERICAL SIMULATION MODEL AND METHOD

2.1. Numerical Simulation Model. To simulate the transient nature of gas—solid flows in the IIFB reactor, a non-steady-state, Eulerian multi-fluid model is used. The gas phase is modeled with the $k-\varepsilon$ turbulent model, and the particle phase is modeled with the kinetic theory of granular flow. The model is based on the fundamental concept of interpenetrating continua for multiphase mixtures.

2.1.1. Continuity Equation. The continuity equations of gas and solid phases are

$$\frac{\partial}{\partial t}(\alpha_g \rho_g) + \nabla(\alpha_g \rho_g \boldsymbol{v_g}) = 0 \tag{1}$$

$$\frac{\partial}{\partial t}(\alpha_s \rho_s) + \nabla(\alpha_s \rho_s \boldsymbol{v_s}) = 0 \tag{2}$$

where α is the void fraction, ρ is the density, and $\boldsymbol{v}$ is the instantaneous velocity of the gas/solid phase. The subscripts g and s denote the gas and solid phases, respectively.

2.1.2. Momentum Equations. The momentum equation of the gas phase is

$$\frac{\partial}{\partial t}(\alpha_g \rho_g \boldsymbol{v_g}) + \nabla(\alpha_g \rho_g \boldsymbol{v_g v_g})$$
$$= -\alpha_g \nabla p_g + \nabla \boldsymbol{\tau_g} - \beta(\boldsymbol{v_g} - \boldsymbol{v_s}) + \alpha_g \rho_g \boldsymbol{g} \tag{3}$$

where $\boldsymbol{\tau_g}$ is the gas-phase stress tensor, β is the drag coefficient of gas—solid flow, and $\boldsymbol{g}$ is the special gravity force. The definitions of $\boldsymbol{\tau_g}$ and β are[29,30]

$$\boldsymbol{\tau_g} = \alpha_g \mu_g [\nabla \boldsymbol{v_g} + (\nabla \boldsymbol{v_g})^T] + \alpha_g \left(\lambda_g - \frac{2}{3}\mu_g\right)(\nabla \boldsymbol{v_g})\boldsymbol{I} \tag{4}$$

$$\beta = \begin{cases} \frac{3}{4} C_D \frac{\alpha_s \alpha_g \rho_g |\boldsymbol{v_s} - \boldsymbol{v_g}|}{d_s} \alpha_g^{-2.65} & \alpha_g > 0.8 \\ 150 \frac{\alpha_s^2 \mu_g}{\alpha_g d_s^2} + 1.75 \frac{\rho_g \alpha_s}{d_s}|\boldsymbol{v_s} - \boldsymbol{v_g}| & \alpha_g \leq 0.8 \end{cases} \tag{5}$$

$$C_D = \begin{cases} \frac{24}{Re_s}[1 + 0.15(Re_s)^{0.687}] & Re_s < 1000 \\ 0.44 & Re_s \geq 1000 \end{cases} \tag{6}$$

$$Re_s = \frac{\alpha_g \rho_g d_s |\boldsymbol{v_g} - \boldsymbol{v_s}|}{\mu_g} \tag{7}$$

In eq 4, μ_g is the effective viscosity and $\boldsymbol{I}$ is the unit tensor. The momentum equation of the solid phase is

$$\frac{\partial}{\partial t}(\alpha_s \rho_s \boldsymbol{v_s}) + \nabla(\alpha_s \rho_s \boldsymbol{v_s v_s}) = -\alpha_s \nabla p_g + \nabla \boldsymbol{\tau_s}$$
$$+ \beta(\boldsymbol{v_g} - \boldsymbol{v_s}) + \alpha_s \rho_s \boldsymbol{g} \tag{8}$$

Table 1. Typical Operating Conditions Used for the Simulation

parameters	value	remarks
particle density (ρ_P)	2500 kg/m^3	quartz sand
gas density (ρ_g)	1.2 kg/m^3	air/N$_2$ (20 °C)
gas viscosity (μ)	1.79 × 10^{-5} Pa s	air/N$_2$ (20 °C)
time step (ΔT)	0.00025 s	set value
pressure (P)	101325 Pa	atmospheric pressure
restitution coefficient between the solid particles	0.97	set value
maximum packing limit	0.58	set value
particle diameter (d_P)	0.3 mm	set value
spouting gas flow rate (U_s)	26.7 m/s	set value
fluidizing gas flow rate (U_f)	0.168 m/s	set value
initial particle volume (V)	900 mL	measurement

where $\boldsymbol{\tau_s}$ is the particle-phase stress tensor defined as the sum of the kinetic stress tensor ($\boldsymbol{\tau_s^k}$) and the frictional stress tensor ($\boldsymbol{\tau_s^f}$).[31]

The kinetic stress tensor is modeled by the kinetic theory of granular flow according to Gidaspow's work.[32] Solid viscosity and pressure are computed via the random fluctuation of solid velocity because of particle–particle collisions. Such a random kinetic energy or granular temperature is obtained by solving a fluctuating kinetic energy equation for the particles additionally. Thus, the solid viscosity and pressure can then be computed as a function of the granular temperature at any time and position. Closure equations for the kinetic stress tensor ($\boldsymbol{\tau_s^k}$) and granular temperature (Θ_s) are listed below

$$\boldsymbol{\tau_s^k} = (-p_s^k + \alpha_s \lambda_s^k (\nabla \boldsymbol{v_s}))\boldsymbol{I} + 2\alpha_s \mu_s^k \boldsymbol{S_s} \tag{9}$$

$$\boldsymbol{S_s} = \frac{1}{2}(\nabla \boldsymbol{v_s} + (\nabla \boldsymbol{v_s})^T) - \frac{1}{3}(\nabla \boldsymbol{v_s})\boldsymbol{I} \tag{10}$$

$$p_s^k = \alpha_s \rho_s \Theta_s + 2\rho_s(1 + e_{ss})\alpha_s^2 g_{0,ss}\Theta_s \tag{11}$$

$$\mu_s^k = \frac{4}{5}\alpha_s \rho_s d_s g_{0,ss}(1 + e_{ss})\left(\frac{\Theta_s}{\pi}\right)^{1/2}$$
$$+ \frac{10\rho_s d_s \sqrt{\Theta_s \pi}}{96(1 + e_{ss})g_{0,ss}}\left[1 + \frac{4}{5}(1 + e_{ss})\alpha_s g_{0,ss}\right]^2 \tag{12}$$

$$\lambda_s^k = \frac{4}{3}\alpha_s \rho_s d_s g_{0,ss}(1 + e_{ss})\left(\frac{\Theta_s}{\pi}\right)^{1/2} \tag{13}$$

$$g_{0,ss} = \frac{1 + 2.5\alpha_s + 4.5904\alpha_s^2 + 4.515439\alpha_s^3}{[1 - (\alpha_s/\alpha_{s,max})^3]^{0.67802}} \tag{14}$$

$$k_{\Theta_s} = \frac{150\rho_s d_s \sqrt{\Theta_s \pi}}{384(1 + e_{ss})g_{0,ss}}\left[1 + \frac{6}{5}\alpha_s g_{0,ss}(1 + e_{ss})\right]^2$$
$$+ 2\alpha_s^2 \rho_s d_s g_{0,ss}(1 + e_{ss})\sqrt{\frac{\Theta_s}{\pi}} \tag{15}$$

$$\gamma_{\Theta_s} = 3(1 - e_{ss}^2)g_{0,ss}\rho_s \alpha_s^2 \Theta_s \left(\frac{4}{d_s}\sqrt{\frac{\Theta_s}{\pi}} - \nabla \boldsymbol{v_s}\right) \tag{16}$$

$$\phi_{sg} = -3\beta\Theta_s \tag{17}$$

2.2. Boundary Conditions and Calculation Method. Fluent 6.3, CFD commercial software, is used to calculate the model. At the gas inlet, velocities of the spouting gas and fluidizing gas are specified. At the outlet, the mass fluxes of both gas and particles are assumed and the pressure is at an ambient atmosphere. Initially, the bed was patched with the solid volume fraction of 0.58, and the velocity of both the gas and solid in the bed are set at zero. At the walls, the no-slip wall conditions are assumed for both gas and solid.

The structure of the reactor is very complicated. It includes a draft tube with some slots at the bottom of the reactor. To obtain reliable simulation results, the side length of the grid should be relatively uniform and the minimum side length should be set to less than the width of the slots at the bottom of the draft tube. The quad unstructured grid was used to generate the mesh of the bottom part of the reactor, and the Cooper grid was used to generate the mesh in the rest of it. The simulation meshes are shown in Figure 2. The number of unstructured meshes is 25 000, while the total amount of meshes is 246 000. Among these meshes, the minimum volume is 1.14 × 10^{-10} m^3 and the maximum volume is 1.79 × 10^{-6} m^3. First-order upwind discretization was used for both momentum and volume fraction solutions. The typical simulation parameters and operating conditions are listed in Table 1. These operating parameters were obtained from the optimal flow conditions of the IIFB reactor observed in our previous experimental study.[27] There is a steady fountain in the pyrolysis bed and bubbling fluidization in the combustion bed under these conditions.

To add resistance to the pyrolysis bed and combustion bed outlets, two small regions close to them are set as porous media regions. Relative resistance coefficients are given to simulate the resistance effect of the two outlets, which is in coincidence with the total pressure loss coefficients of the two outlets in the experiments.

3. EXPERIMENTAL SECTION

The schematic diagram of the experimental setup is shown in Figure 3, which was described elsewhere.[27] This system mainly consists of an IIFB unit, a gas supply system, and some measurement and control instruments. The main body of the IIFB unit is made of Plexiglas and consists of three concentric semi-cylinders, i.e., a draft tube, a dipleg, and an outer wall. The inner diameter of the bed is 100 mm, and it is divided by two flanges into three parts with heights of 100 mm (windbox), 800 mm (annulus region), and 600 mm (fountain region). A gas distributor with 2 mm holes and an opening area ratio of 1.6% is located at the bottom of the annulus. A sheet of steel screen (200 mesh) is used to cover the distributor and to prevent the bed materials from falling into the windbox. The draft tube with three slots at the bottom is 900 mm in height and 24 mm in inner diameter. The width and height of the slots are 5 and 50 mm, respectively. The spouting gas is introduced by a spout tube with an inner diameter of 11 mm. A conical plate with an inclined angle of 45° and a dipleg with an inner diameter of 39 mm are installed between the draft tube and the bed. The distance between the dipleg and distributor is 150 mm.
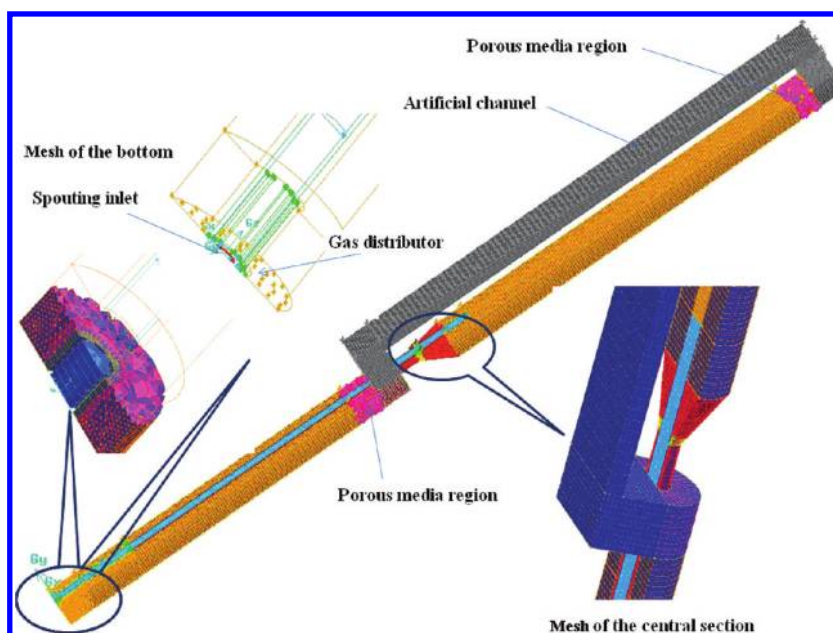
Figure 2. Picture of the simulation meshes.

The spouting and fluidizing gases are supplied by an air compressor. The gas flow rates are measured by two flow meters. The spouting gas is introduced into the bed directly through the draft tube, while the fluidizing gas first enters the windbox and then enters the bed via the holes in the gas distributor. All of the gases are dehydrated in a dehydrator before being used.

There are two outlets in the IIFB system, i.e., the pyrolysis gas outlet and combustion gas outlet. Therefore, the resistances of the following equipments after the two outlets (such as cyclones, condensers, valves, etc.) have significant effects on the flow characteristics of particles in the IIFB reactor. In the experimental study, we located two valves at the two outlets to simulate the two resistances. The resistances of the following equipments after the two outlets were adjusted by the opening values of the two valves. A parameter, named total pressure loss coefficient (K), was introduced to represent the residence of the outlet. Its definition is shown in eq 18

$$K = \sum_{i}^{n} \zeta_i \frac{A_t^2}{A_i^2} + \sum_{j}^{m} \lambda_j \frac{l_j}{d_j} \frac{A_t^2}{A_j^2} + \xi_g \frac{A_t^2}{A_g^2} + \xi_s \frac{A_t^2}{A_s^2} \quad (18)$$

where ζ_i, ξ_g, and ξ_s are the local resistance coefficient, the resistance coefficient of the valve, and the cyclone separator resistance coefficient, respectively. λ_j, l_j, and d_j are the on-way resistance coefficient, pipeline length, and pipeline diameter, respectively. A_t is the cross-section area of the bed. A_i, A_j, A_g, and A_s are the conversion areas at the corresponding resistance loss units. As shown in eq 18, the K value is determined by the characteristics of an exit and has no relationship with the operating velocity.

K can be calculated by the following equation:

$$K = \frac{2\Delta P}{\rho_0} \left(\frac{A_t}{Q}\right)^2 \quad (19)$$

where ΔP is the pressure drop before and after an exit, Q is the gas flow rate, and ρ_0 is the density of air.

In this study, the total pressure loss coefficient of the combustion bed outlet K_c was set at 4570 and that of the pyrolysis bed outlet K_p was set at 25 673. The chosen K_c and K_p values are from the experimental study.

The solid circulation rate of the IIFB reactor was obtained by measuring the particle downward velocity in the dipleg. Some sand particles with the same particle diameter as bed materials were
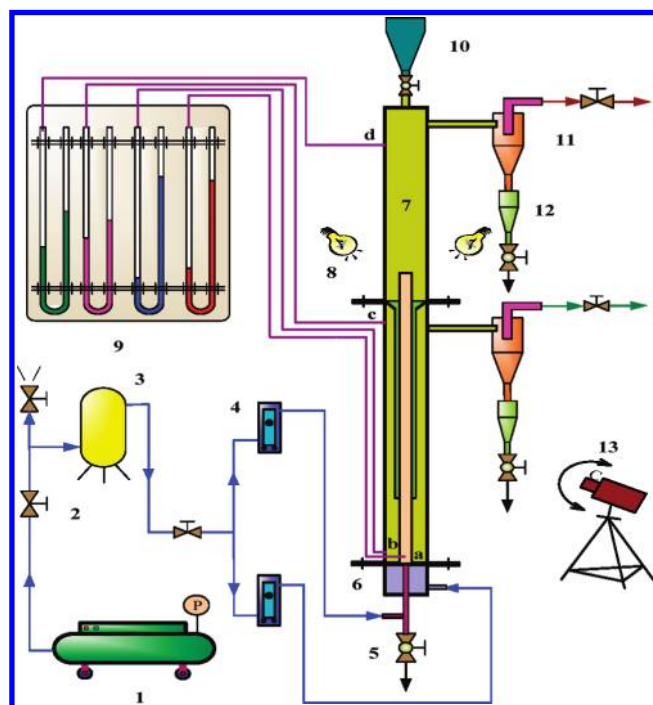

Figure 3. IIFB experimental system of the internally interconnected fluidized beds (1, air compressor; 2, gate valve; 3, dehydrator; 4, rotameter; 5, ball valve; 6, windbox; 7, IIFB system; 8, floodlight; 9, U-type manometer; 10, bed materials feed tank; 11, cyclone separator; 12, fines collector; 13, digital CCD; a, b, c, d. Pressure measurement points).

dyed black and used as tracer particles. Because the flow of the bed materials in the dipleg was similar to that in a moving bed, the velocities of the tracer particles could represent the bulk velocity of the bed materials in the dipleg. According to the particle velocity and the area of the cross-section of dipleg, the solid circulation rate can be obtained.
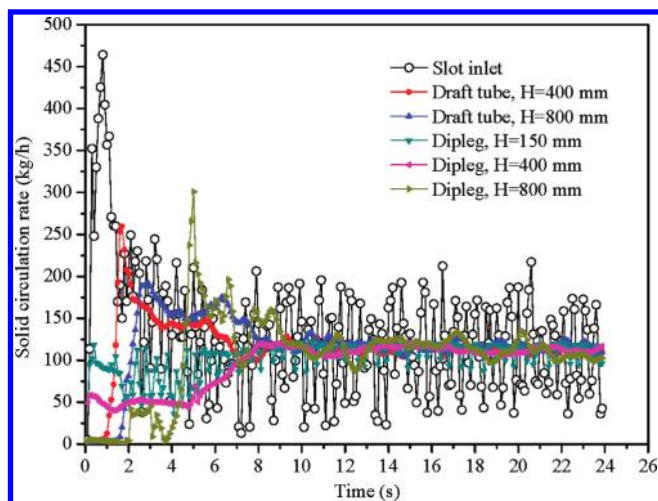
Figure 4. Solid circulation rate as a function of the computational time on stream at the different cross-sections.

Figure 5. Pressure as a function of the computational time on stream at the different positions.

4. RESULTS AND DISCUSSION

4.1. Solid Circulation Rate as a Function of the Computational Time on Stream at Different Positions. Figure 4 shows the solid circulation rate as a function of the computational time at the slot inlet, different cross-sections of the draft tube, and dipleg. As can see from the figure, the solid circulation rate calculated by the amount of the particles passing through the draft tube cross-sections is higher than that through the dipleg at the beginning. This can be explained by the fact that the particles are rising, whereas less particles are falling down, and the particle circulation is not built. After 12 s, the solid circulation rate calculated at the cross-sections of the draft tube and dipleg are converged as the same value of about 110 kg/h. This result means that the amount of upward particles in the draft tube is equal to that of downward particles in the dipleg. The circulation is well-built, and the steady spouting is formed. We measured the solid circulation rate at the same operating conditions in the IIFB experimental system. The result shows that the solid circulation rate is 104.5 kg/h. The simulation result is in well-agreement with experimental data. Bubbles generating and shattering in the annulus lead to particle velocity fluctuation at the slot inlet. Therefore, the solid circulation rate shows a periodical variation.

4.2. Pressure as a Function of the Computational Time at Different Positions. Figure 5 shows the pressure as a function of the computational time at the three different cross-sections: the bottom of IIFB, the pyrolysis bed, and the combustion bed outlets (before porous media regions). As can be seen from the figure, the pressure is unstable for the first 12 s. At this transient period, the fountain above the dipleg is formed. After 12 s, the pressure fluctuates around a constant (the fitting line in the figure) with computational time on stream. This also means that the flow attains a steady stage after 12 s, which is coincident with the conclusion obtained from the simulation results of the solid circulation rate. The values of fitting lines at the bottom of IIFB, the pyrolysis bed, and the combustion bed outlets are 3250, 1750, and 390 Pa, respectively. These fitting line values can be regarded as the time-averaged values at stable flow, which can be used for design and analysis of the fluidization process. We have performed the pressure measured experiments in our previous study.[27] The pressures at the bottom of IIFB, the pyrolysis bed, and the
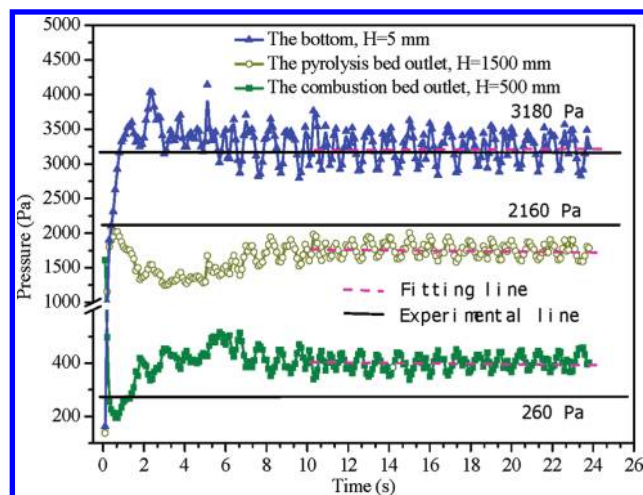
combustion bed outlets are 3180, 2160, and 260 Pa, respectively. The experimental data of the pressures are close to that obtained by simulation.

4.3. Solid Volume Fraction. Figure 6 shows the development of the solid volume fraction in the IIFB reactor with computational time on stream. The particles are quiescent at 0 s. Some particles are entrained into the draft tube by spouting gas and flowing up at 1 s. The annular region becomes unstable, and bubbles begin to generate because of the fluidizing gas blowing. The particles are continuously entrained into the draft tube, and the particles in the tube continuously ascend with computational time on stream, whereas the particles in the dipleg begin to glide down because of the increase of the voidage of the annulus. At 2 s, the particles arrive at the top of the draft tube and form spouting at the exit. At 8 s, the particles fall along the dipleg because of their gravity and assemble above the conical plate to supply the solids to glide down into the combustion bed. The fountain height and profile tend to be almost constant after 12 s. Stable flows of solid and gas phases are obtained when the time is over 12 s. This result is consistent with the simulation results for solid circulation and pressure. The experimental study was conducted under the same operating conditions. The results show that the spouting phenomenon was continuous and the height and profile of the fountain were kept the same. The picture of one random moment was taken and shown in Figure 6 to compare to the simulation results. As can be seen in the figure, in both the simulation and experiment, (1) the particles in the combustion bed are fluidized, (2) the particles are entrained at the bottom of the draft tube through the slots, and (3) the particles pass through the drat tube and form a fountain.

From the above study, we can conclude that a steady fountain can be formed in the new reactor. After attaining a steady stage, the parameters change little. Therefore, we can use instantaneous values to investigate the flow characteristics. According to simulation results, the flow attains stability after 12 s of computational time. We used instantaneous values at 20 s in the following study.

4.4. Pressure Distribution. The pressure distributions on different cross-sections are shown in Figure 7. The use of porous media regions causes the increase of the pressure before them. The pressure decreases suddenly when the gas passes through the porous media regions, which reflects the influence of valve
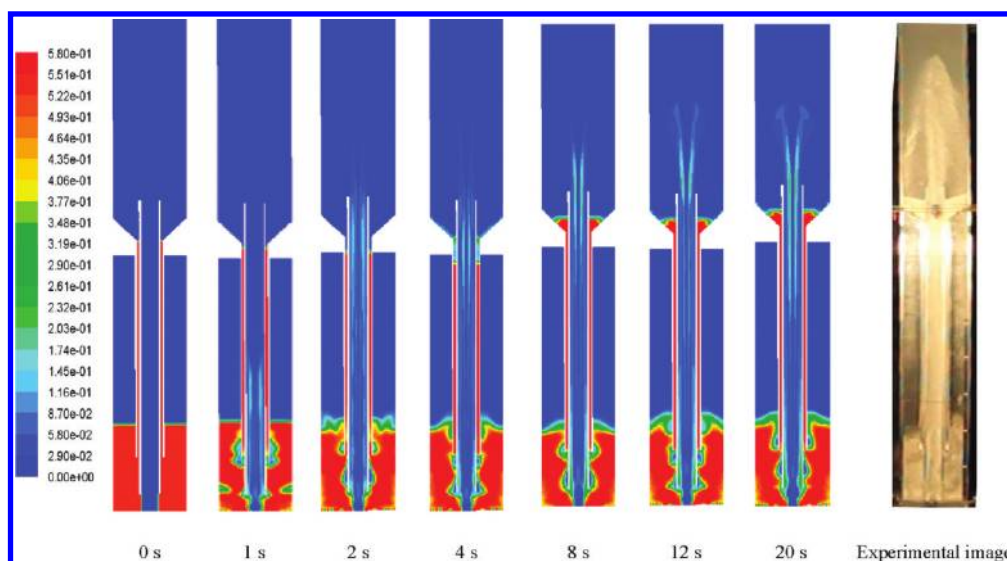
Figure 6. Development of the solid volume fraction in the IIFB reactor with computational time on stream.
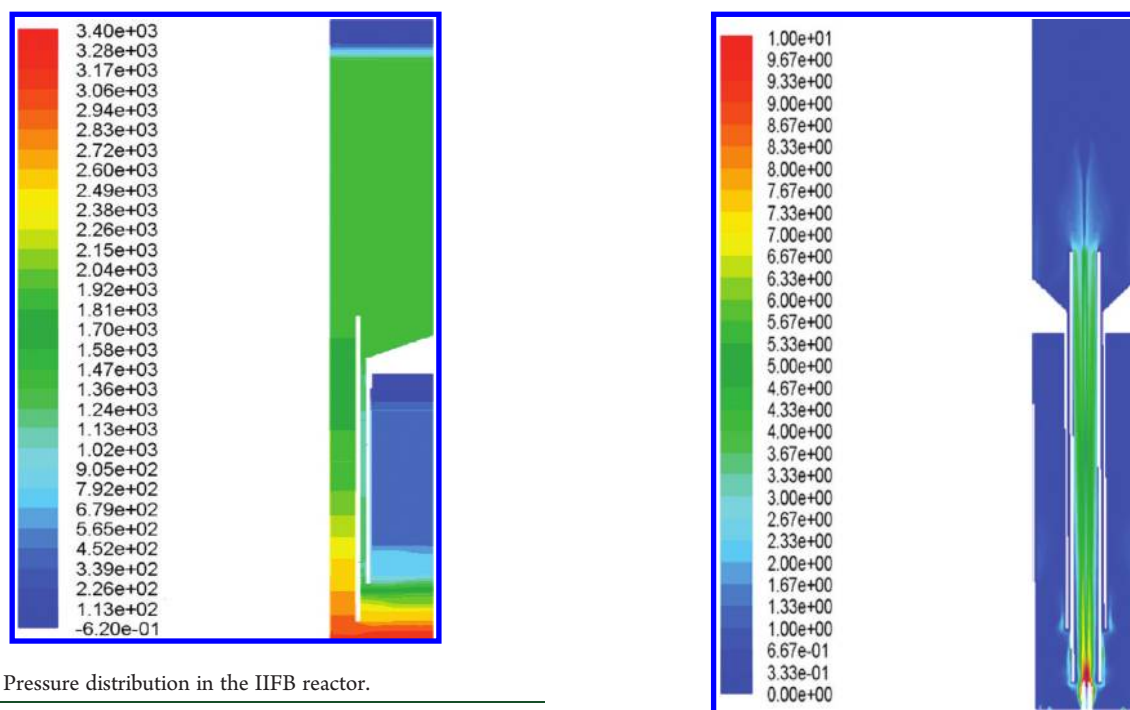

Figure 7. Pressure distribution in the IIFB reactor.

Figure 8. Velocity magnitude of the gas phase.

resistances. The region near the distributor and the inlet of the draft tube presents the highest pressure. The pressure shows a reducing tendency in the draft tube and fluidization zone with the increase of the height at the particle existing regions. The pressure near the pyrolysis bed outlet is obviously higher than that near the combustion bed outlet. Thus, just very little fluidizing gas can bypass into the pyrolysis bed through the slots from the combustion bed.

4.5. Velocity Magnitude of Gas and Solid in the IIFB System. Velocity magnitudes of the gas and solid phases are shown in Figures 8 and 9, respectively. The velocity magnitude is defined as $U = (U_x^2 + U_y^2 + U_z^2)^{1/2}$. It can be seen from the figures that the spouting gas velocity is quite large at the inlet and then decreases sharply because of jet expansion and gas bypassing to the annulus through the slots. The solid velocity magnitude first

decreased along the height of the draft tube and then was kept as a constant. Above the draft tube, the gas velocity decreases markedly because of another jet expansion. In the fountain region, the gas still rises until it is out of the reactor from the pyrolysis bed outlet, whereas the solid first rises and then falls into the dipleg to complete the circulation.

4.6. Particle Vertical Velocity Profile at Different Heights. Particle vertical velocity profiles at different heights are shown in Figure 10. In the draft tube, the vertical velocity of the particles first underwent a disturbed flow because of the solid—solid and solid—wall collisions (position A), then increased rapidly, and last was kept at almost a uniform magnitude (position B). After the particles leave the draft tube, they lose their momentum in
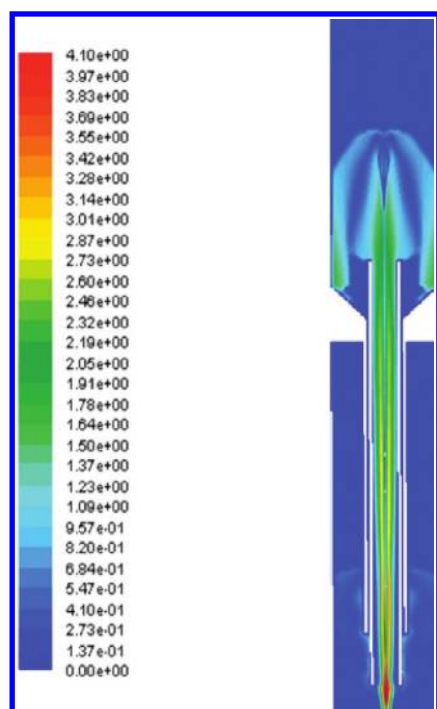
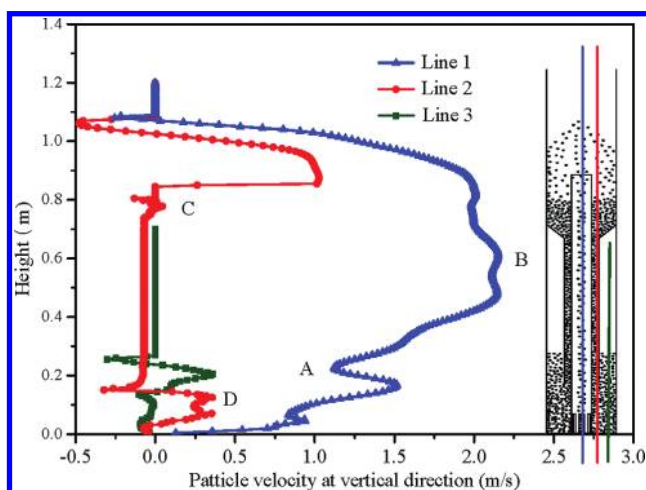**Figure 9.** Velocity magnitude of the solid phase.

Figure 10. Particle vertical velocity profile at different heights.

the vertical direction, which results in a significant decrease in vertical velocity. When they arrive at the highest point, the particles start to move along the reverse direction after the complete loss of momentum. In the dipleg, the particles glide down with a constant velocity of 0.07 m/s. Before the particles enter the dipleg, they assemble on the conical plate and form a unstable velocity region C. At the bottom of the dipleg, the particles move to the annulus and start to show a large fluctuation in velocity, depicted as region D in Figure 10. The above flow patterns and characteristics estimated from simulations coincide well with experimental results.

5. CONCLUSION

A three-dimensional, non-steady-state, Eulerian multi-fluid model with the $k-\varepsilon$ turbulent model for the gas phase and the kinetic theory of granular flow for the solid phase was used to study the gas—solid flow behaviors in a novel catalytic fast pyrolysis reactor. The experiment was carried out in a cold-stage experimental system. The conclusions are summarized as follows: (1) The simulation results about the solid circulation rate and pressure are in good agreement with the experimental results, which means the model was built successfully. The porous regions close to the two outlets of the reactor, where pressure decreases suddenly when gas passed through the porous regions, can model the residences of two outlets. (2) After the particles are entrained into the draft tube, they have a very high horizontal momentum, followed by a remarkable decrease probably because of solid—solid and solid—wall collisions. The particles in the dipleg were monitored to drop downward at a uniform speed of 0.07 m/s. This indicates that the dipleg acts as a moving bed, preventing the gas bypassing between the pyrolysis bed and combustion bed.

■ AUTHOR INFORMATION

Corresponding Author
*E-mail: ruixiao@seu.edu.cn.

■ NOMENCLATURE

A_t = cross-section area of the whole bed (C)
A_i = conversion area at local resistance loss unit (m^2)
A_j = conversion area at on-way resistance loss unit (m^2)
A_g = conversion area at a valve (m^2)
A_s = conversion area at the cyclone separator (m^2)
C_D = drag coefficient
d_j = pipeline diameter (m)
d_s = particle diameter (m)
e_{ss} = particle—particle collision restitution coefficient
g = special gravity force (m/s^2)
$g_{0,ss}$ = radial distribution function
I = unit tensor
K = total pressure loss coefficient of an exit
K_c = total pressure loss coefficient of the combustion bed exit
K_P = total pressure loss coefficient of the pyrolysis bed exit
k_{Θ_s} = transport coefficient of pseudo-thermal energy (kg m^{-1} s^{-2})
l_j = pipeline length (m)
p_s^k = kinetic pressure in the solid phase (N m^{-2})
ΔP = pressure drop before and after an exit (Pa)
Q = gas flow rate (m^3/h)
Re_s = Reynold's number
S_s = particle strain rate tensor (s^{-1})
U = velocity magnitude (m/s)
U_x = velocity magnitude at the x axis (m/s)
U_y = velocity magnitude at the y axis (m/s)
U_z = velocity magnitude at the z axis (m/s)
ν_g = instantaneous velocity of gas (m/s)
ν_s = instantaneous velocity of solid (m/s)

Greek Letters

α_g = void fraction of gas
α_s = void fraction of solid
β = drag coefficient of gas−solid flow
γ_{Θ_s} = dissipation of pseudo-thermal energy through inelastic collisions (kg m^{-1} s^{-3})
Θ_s = granular temperature
λ_i = on-way resistance coefficient
λ_s^k = solid-phase bulk viscosity (kg m^{-1} s^{-1})
μ_g = effective viscosity
μ_s^k = kinetic viscosity in the solid phase (kg m^{-1} s^{-1})
ρ_0 = air density (kg/m^3)
ρ_g = density of gas (kg/m^3)
ρ_s = density of solid (kg/m^3)
τ_g = gas-phase stress tensor
τ_s = particle-phase stress tensor
τ_s^k = kinetic stress tensor
τ_s^f = frictional stress tensor
ϕ_{sg} = exchange of fluctuating energy between gas and particles (kg m^{-1} s^{-3})
ζ_i = local resistance coefficient
ξ_g = resistance coefficient of a valve
ξ_s = resistance coefficient of the cyclone separator

Subscripts

g = gas phase
s = solid phase
max = maximum
min = minimum

■ REFERENCES

(1) Kunkes, E. L.; Simonetti, D. A.; West, R. M.; Serrano-Ruiz, J. C.; Gartner, C. A.; Dumesic, J. A. *Science* **2008**, *322*, 417–421.
(2) Huber, G. W.; Iborra, S.; Corma, A. *Chem. Rev.* **2006**, *106* (9), 4044–4098.
(3) Vispute, T. P.; Zhang, H. Y.; Sanna, A.; Xiao, R.; Huber, G. W. *Science* **2010**, *330*, 1222–1227.
(4) Demirbas, A. *Energy Convers. Manage.* **2001**, *42* (11), 1357–1378.
(5) Klass, D. L. *Fuels and Chemicals*; Academic Press: New York, 1998.
(6) Sims, R. E. H.; Hastings, A.; Schlamadinger, B.; Taylor, G.; Smith, P. *Global Change Biol.* **2006**, *12* (11), 2054–2076.
(7) Luque, R.; Herrero-Davila, L.; Campelo, J. M.; Clark, J. H.; Hidalgo, J. M.; Luna, D.; Marinas, J. M.; Romero, A. A. *Energ. Environ. Sci.* **2008**, *1* (5), 542–564.
(8) Anex, R. P.; Aden, A.; Kazi, F. K.; Fortman, J.; Swanson, R. M.; Wright, M. M.; Satrio, J. A.; Brown, R. C.; Daugaard, D. E.; Platon, A.; Kothandaraman, G.; Hsu, D. D.; Dutta, A. *Fuel* **2010**, *89*, S29–S35.
(9) Bridgwater, A. V. *J. Anal. Appl. Pyrolysis* **1999**, *51* (1−2), 3–22.
(10) Bridgwater, A. V.; Meier, D.; Radlein, D. *Org. Geochem.* **1999**, *30* (12), 1479–1493.
(11) Czernik, S.; Bridgwater, A. V. *Energy Fuels* **2004**, *18* (2), 590–598.
(12) Lappas, A. A.; Samolada, M. C.; Iatridis, D. K.; Voutetakis, S. S.; Vasalos, I. A. *Fuel* **2002**, *81* (16), 2087–2095.
(13) Lappas, A. A.; Dimitropoulos, V. S.; Antonakou, E. V.; Voutetakis, S. S.; Vasalos, I. A. *Ind. Eng. Chem. Res.* **2008**, *47* (3), 742–747.
(14) Atutxa, A.; Aguado, R.; Gayubo, A. G.; Olazar, M.; Bilbao, J. *Energy Fuels* **2005**, *19* (3), 765–774.
(15) Xiao, R.; Zhang, M. Y.; Jin, B. S.; Liu, X. D. *Can. J. Chem. Eng.* **2002**, *80* (5), 800–808.
(16) Aguado, R.; Olazar, M.; Jose, M. J. S.; Aguirre, G.; Bilbao, J. *Ind. Eng. Chem. Res.* **2000**, *39* (6), 1925–1933.
(17) Zhang, H. Y.; Xiao, R.; Wang, D. H.; Zhong, Z. P.; Song, M.; Pan, Q. W.; He, G. Y. *Energy Fuels* **2009**, *23*, 6199–6206.
(18) Zhang, H. Y.; Xiao, R.; Huang, H.; Xiao, G. *Bioresour. Technol.* **2009**, *100* (3), 1428–1434.
(19) Carlson, T. R.; Cheng, Y. T.; Jae, J. H.; Huber, G. W. *Energy Environ. Sci.* **2011**, *4* (1), 145–161.
(20) Aho, A.; Kumar, N.; Eranen, K.; Salmi, T.; Hupa, M.; Murzin, D. Y. *Fuel* **2008**, *87* (12), 2493–2501.
(21) Aho, A.; Kumar, N.; Eranen, K.; Salmi, T.; Hupa, M.; Murzin, D. Y. *Process Saf. Environ.* **2007**, *85* (B5), 473–480.
(22) Lin, Y. C.; Huber, G. W. *Energy Environ. Sci.* **2009**, *2* (1), 68–80.
(23) Jae, J.; Tompsett, G. A.; Foster, A. J.; Hammond, K. D.; Auerbach, S. M.; Lobo, R. F.; Huber, G. W. *J. Catal.* **2011**, *279* (2), 257–268.
(24) Jae, J. H.; Tompsett, G. A.; Lin, Y. C.; Carlson, T. R.; Shen, J. C.; Zhang, T. Y.; Yang, B.; Wyman, C. E.; Conner, W. C.; Huber, G. W. *Energy Environ. Sci.* **2010**, *3* (3), 358–365.
(25) Bridgwater, A. V. *Chem. Eng. J.* **2003**, *91* (2−3), 87–102.
(26) Mohan, D.; Pittman, C. U.; Steele, P. H. *Energy Fuels* **2006**, *20* (3), 848–889.
(27) Zhang, H. Y.; Xiao, R.; Pan, Q. W.; Song, Q. L.; Huang, H. *Chem. Eng. Technol.* **2009**, *32* (1), 27–37.
(28) Goldschmidt, M. J. V.; Beetstra, R.; Kuipers, J. A. M. *Chem. Eng. Sci.* **2002**, *57* (11), 2059–2075.
(29) Huilin, L.; Gidaspow, D.; Bouillard, J.; Wentie, L. *Chem. Eng. J.* **2003**, *95* (1−3), 1–13.
(30) Gunn, D. J. *Int. J. Heat Mass Transfer* **1978**, *21* (4), 467–476.
(31) Savage, S. B. *J. Fluid Mech.* **1998**, *377*, 1–26.
(32) Gidaspow, D. *Multiphase Flow and Fluidization: Continuum and Kinetic Theory Descriptions*; Academic Press: New York, 1994.